

Binary Level-Set Shape Optimization Model and Algorithm for Volumetric Modulated Arc Therapy in Cancer Radiotherapy

Li-Tien Cheng^{*} Bin Dong[†] Chunhua Men[‡] Xun Jia[‡]
Steve Jiang[‡]

August 13, 2012

Abstract

Radiation therapy is one of the most commonly used treatment modalities for cancer. Its purpose is to deliver prescribed radiation doses to cancerous targets using high energy radiation beams while sparing nearby healthy organs. The treatment planning process of radiotherapy is an optimization problem, where beam parameters, such as directions, shapes, and intensities, can be adjusted in simulations to yield desired dose distributions. This can be applied under the recently developed volumetric modulated arc therapy (VMAT) setup which involves the use of a full-rotation trajectory of the beam about the patient along with a multi-leaf collimator for beam shape sculpting, with notable advantages in shortened treatment time. Treatment plan optimization in this setting, however, can be quite complicated due to constraints arising from the equipment involved. We introduce a variational model in the VMAT setup for the optimization of

^{*}Department of Mathematics, University of California, San Diego, 9500 Gilman Drive, Mail code: 0112, La Jolla, CA 92093-0112, Email: lcheng@math.ucsd.edu

[†]Department of Mathematics, University of Arizona, 617 N. Santa Rita Ave, Tucson, AZ, 85721-0089, Email: dongbin@math.arizona.edu

[‡]Center for Advanced Radiotherapy Technologies and Department of Radiation Medicine and Applied Sciences, University of California, San Diego, 3855 Health Sciences Drive, Mail code: 0843, La Jolla, CA 92093-0843, Email: {cmen, xunjia, sbjiang}@ucsd.edu

beam shapes and intensities under these constraints. We apply a binary level-set strategy to represent beam shapes and a fast sweeping technique to satisfy beam intensity variation limits. The result is a flow-based shape optimization algorithm that guarantees constraint satisfaction and energy decrease for the generation of improved treatment plans in VMAT. Simulations of clinical cases are included to validate our algorithm.

1 Introduction

1.1 Cancer and Radiotherapy

Cancer is a class of diseases in which a group of cells display uncontrolled growth, invasion, and sometimes metastasis. According to the World Health Organization, cancer is a leading cause of death worldwide, accounting for around 7.5 million deaths (around 13% of all deaths) per year (<http://www.who.int/mediacentre/factsheets/fs297/en/>). According to the US National Cancer Institute, there are an estimated 1.6 million new cancer cases causing 0.58 million deaths in the United States in 2012 (<http://www.cancer.gov/cancertopics/what-is-cancer>). Cancer is thus one of the dominant health issues of our society today.

This naturally drives a demand for advances in cancer treatment. Along with chemotherapy and surgery, radiation therapy is one of the three main modalities of cancer treatment. It is estimated that, in the United States, over 60% of cancer patients are treated with radiation therapy at some point of their cancer management. The purpose of radiation therapy is to deliver sufficient dose to the cancerous tissue (target) while staying within acceptable dose levels for critical healthy tissues and organs.

The most common type of radiation therapy utilizes a medical linear accelerator, mounted on a gantry that can rotate around the patient, to generate high energy (4–20 MeV range) radiation. The radiation beams are collimated into desired shapes through a device called the multi-leaf collimator (MLC) before hitting the patient. A typical MLC, as shown in Figure 1.1, consists of 60 pairs of tungsten leaves, with each leaf being able to move back and forth, driven by a motor and controlled by a computer algorithm.

Since radiation can cause harm to normal tissues, a balance must be achieved between sufficient dose to a cancerous target and minimal dose to healthy tissues. In modern radiation therapy, this is finalized in the treatment

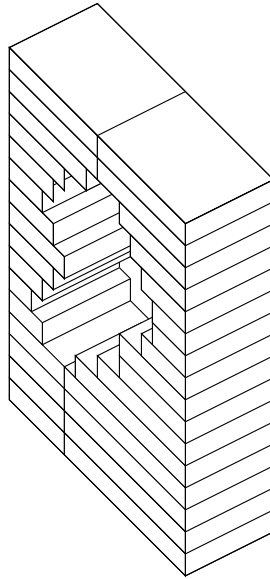


Figure 1.1: Diagram of a multi-leaf collimator (MLC) opening and closing its leaves to produce shapes that sculpt radiation beams passing through.

planning stage, where treatment parameters, such as beam direction, intensity, duration, and shape, for optimal dose distributions are computed prior to treatment. One approach is then to designing an energy function, assisted by knowledge of patient anatomy from the image processing of computed-tomography (CT) scans, that weighs desired doses at the target with those at healthy organs. This energy can then be minimized through the use of advanced algorithms, yielding treatment parameters for an optimal dose distribution.

1.2 Volumetric Modulated Arc Therapy

Volumetric modulated arc therapy (VMAT) [1–5] has recently become a very popular treatment modality in radiation therapy. In VMAT, the gantry is rotated around the patient, while beam intensities and shapes are varied continuously (see Figure 1.2 for an illustration). At each beam angle during the rotation, the MLC forms a predesigned shape, which we call an aperture shape, that sculpts radiation beams passing through of predesigned intensity. Compared to conventional intensity-modulated radiation therapy

(IMRT), where beams are delivered at only a few (e.g. 7) beam angles and a complicated set of beam apertures are designed at each beam angle, VMAT can deliver dose distributions of similar or better quality [6–15]. In addition, VMAT significantly shortens treatment times, completing treatment in a single rotation of the gantry. This not only reduces patient treatment time, thus increasing the availability of the treatment machines for all, but also serves to diminish errors caused by patient motion during the radiation treatment. Thus, it is not surprising that VMAT is generally considered one of the most promising radiotherapy technologies currently available, with great potential in improving treatment outcome in the face of limited resources.

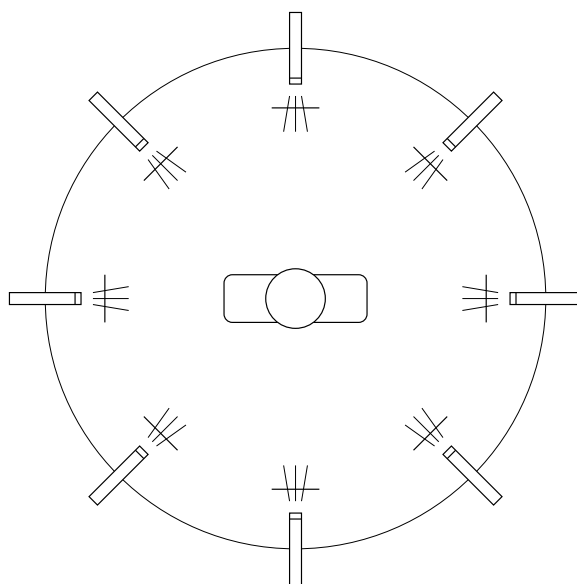


Figure 1.2: Illustration of VMAT treatment delivery: the machine gantry rotates around the patient while beams, shaped by MLC prior to arrival at the patient location, deliver radiation doses.

1.3 Complexities

Significant improvement in VMAT treatment, however, is challenged by the complexities of treatment plan optimization, where treatment parameters are subject to strong constraints due to mechanics of the equipment involved. It becomes a challenge just to describe the constraints underlying

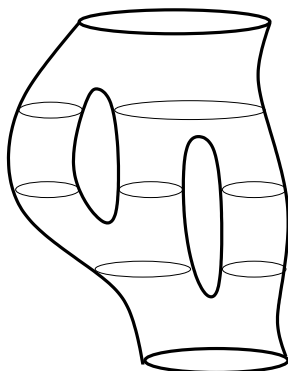


Figure 1.3: An example of an aperture configuration plotted with vertical axis the gantry angle and horizontal planes the MLC plane. Following the gantry rotation, the MLC has to deal with an aperture that starts as one connected component, then breaks into two and three components, before merging back together into two and finally one component.

this optimization problem in a clean and precise mathematical language, let alone solve the problem. Over the years, many heuristic approaches have been developed and applied in clinical practice [1–5, 16–19].

One example of the complexity involved can be seen in the parameter of aperture shape, which forces the optimization problem to include a shape optimization component. The aperture shape openings are in fact three-dimensional domains, since they form a two-dimensional domain at each gantry angle, and can take on complex topologies. In fact, the shape may start out at a certain gantry angle as one connected component that later can break apart into several components before finally merging back together into one again (see Figure 1.3). These topologies are partially controlled, though not in a simplifying manner, by constraints imposed by the equipment. Most notably, MLC’s use of leaves oriented in a certain direction forces deliverable aperture shapes to satisfy a sort of directional-convexity. Furthermore, limits on the speed that leaves can open and close force bounds on first derivatives in the gantry angle direction at aperture boundaries. These constraints represent further complexities that still allow complex behaviors such as the merging and breaking described above to occur. In addition, apart from aperture shapes, there can be added constraints on beam intensities during the gantry rotation such as a limit on how fast they can be changed.

Thus a major challenge in generating treatment plans using VMAT to its

full potential is the complexity of the three-dimensional shape optimization with constraints problem. Our approach in facing this challenge will be to ground the problem in a solid mathematical framework, one that is comfortable with geometric shapes, and attack it with advanced mathematical techniques.

1.4 Statement of Problem

With these given background and observations, we can now definitively state the problem of interest in this paper. Given CT scans of patient geometry, with target and critical structures identified by image processing algorithms, we seek to style an improved treatment plan for an individual patient by constructing the parameters that optimize dose distributions under VMAT. We simplify the problem by considering just the parameters of aperture shapes and beam intensities and just the constraints on MLC-created shapes, leaf speeds, and beam intensity speeds. We feel this setup includes a major portion of the key ingredients and complexities of VMAT and the solution of the optimization problem in this setting would represent a solid first step towards our goal of improved radiotherapy treatments. Additional considerations are left to future work.

Our approach begins with the introduction of an energy that weighs the benefits of different dose distributions. These dose distributions are calculated for given aperture shapes and beam intensities within the VMAT setup according to the physics of interactions between radiation and human tissues. We adopt within this framework a binary level-set representation of aperture shapes to deal with their complex topologies, constraints, and deformations, the latter for a flow-based iterative strategy. In fact, we choose to actively enforce energy decrease through the rejection of changes that increase the energy and the modification of stepsizes. Finally, we compute a velocity for a minimizing flow for beam intensities, and modify it using fast sweeping techniques to satisfy constraints. All these add together to form our algorithm for constructing optimal treatment plans.

To study the quality of dose distributions, we turn to the dose-volume histogram (DVH) that plots the percentages of different structures dosed at different levels. The DVH approach has been widely used in radiotherapy clinical practice for quantitative information on whether most or all of a target structure is dosed at acceptable levels and whether most or all of a critical structure is dosed at safe levels. We use the DVH to check our dose distribu-

tions, make slight improvements to them by adjusting weights introduced by our energy, and compare them meaningfully to results from other treatment setups and algorithms. In addition, we inspect our final aperture shapes and beam intensities to confirm that the necessary constraints are satisfied. Such studies serve to verify the efficacy of our algorithms and the quality of their constructed treatment plans.

2 Variational Model

2.1 Energy

Let $S_r, r = 1, \dots, n_S$ denote certain identified structures of interest in the patient's body. Each S_r is a union of coordinates in $x \in \mathbb{R}^3$. For each S_r , let an associated value m_r be given. Structure such as normal tissues and organs, called critical structures, will have m_r equal to the maximum safe dosage level while structures that are cancerous, called target structures, have m_r equal to the dose level necessary to kill the cells. Then given a dose distribution $z(x), x \in \mathbb{R}^3$ defined over the patient's body, we construct for each structure, S_r , the energy functional

$$F_r(z) = \int_{S_r} p_r(z(x)) dx, \quad (2.1)$$

where

$$p_r(z) = \alpha_r(\max\{0, m_r - z\})^2 + \beta_r(\max\{0, z - m_r\})^2$$

and α_r, β_r are constant parameters. This functional weighs how far the dose z is from m_r .

Note the expression for p_r at dose z simplifies to $p_r(z) = \alpha_r(z - m_r)^2$ when $z \leq m_r$ and $p_r(z) = \beta_r(z - m_r)^2$ when $z \geq m_r$. Thus the parameter α_r controls the penalty on doses less than m_r and β_r controls the penalty on doses greater than m_r . For critical structures, we choose $\alpha_r = 0, \beta_r > 0$ so there is no penalty on administering less radiation than the maximum allowed but there is a penalty on exceeding it. For target structures, we choose $\alpha_r > 0, \beta_r > 0$ so there is a penalty as long as the dose administered is not equal to m_r . Note $\beta_r = 0$, allowing arbitrarily high doses on target structures, may seem acceptable but can in reality cause undue harm to healthy cells misidentified during either the image segmentation or manual physician inspection stages of target structure identification. We also note, in

practice, that the penalties α_r, β_r and even the threshold m_r can be adjusted for desired results.

A total energy functional in terms of the dose distribution can then be constructed by summing together the energies of each individual structure:

$$E(z) = \frac{1}{2} \sum_{r=1}^{n_S} F_r(z).$$

Note $E \geq 0$, while $E = 0$ describes the perfect case where target structures are dosed exactly at desired levels, $z = m_r$, and the doses of critical structures are kept at safe levels, $z \leq m_r$.

For simplicity, let us consider a VMAT treatment case where beams are continuously delivered in a circular arc labeled by gantry angle $\theta \in [0, 2\pi]$ and note that our approach can be generalized to other gantry paths. Under the VMAT setup, let $s(\theta)$ denote the beam intensity at each gantry angle $\theta \in [0, 2\pi]$ and $\Omega(\theta)$ be the aperture formed by the MLC at that angle. Then the dose distribution under these beam intensities and apertures takes the form

$$z(x) = \int_0^{2\pi} \int_{\Omega(\theta)} D(x, y, \theta) s(\theta) dy d\theta, \quad (2.2)$$

where $D(x, y, \theta)$ is a dose deposition coefficient detailing the dose received by location x in the body due to a beamlet of radiation with unit intensity passing through location y in the MLC plane, where the aperture exists. This coefficient $D(x, y, \theta)$ is available for the treatment plan optimization problem, and is computed for the specific patient according to physics and biology principles.

The total energy then, as a function of the collection of aperture shapes $\Omega = \{(y, \theta) | y \in \Omega(\theta)\}$ and beam intensities s in the VMAT setup, takes the form

$$E(\Omega, s) = \frac{1}{2} \sum_{r=1}^{n_S} \int_{S_r} p_r \left(\int_0^{2\pi} \int_{\Omega(\theta)} D(x, y, \theta) s(\theta) dy d\theta \right) dx. \quad (2.3)$$

We note that henceforth, we reserve the use of the notation x for locations in the patient body, y for locations in the MLC plane, and θ for gantry angle.

2.2 Level-Set Form

In addition, in place of Ω , we consider a binary level-set representation of the shape [20–22]. The level-set representation [23] has been applied to a host

of interface deformation problems in mathematical applications (see [24]). In this framework, a shape such as that created by the MLC, is replaced by a generally continuous function defined over the ambient space, and usually labeled by ϕ , satisfying $\phi < 0$ inside the shape and $\phi > 0$ outside the shape. In our case, this means

$$\phi : \mathbb{R}^2 \times [0, 2\pi] \rightarrow \mathbb{R},$$

where $\{(y, \theta) | \phi(y, \theta) < 0\}$ represents the aperture opening and $\{(y, \theta) | \phi(y, \theta) = 0\}$ the boundary of this opening (see Figure 2.1). Level-set methods may then tack on a variable of time t in ϕ to capture the flow of the boundary or interface of interest through evolution of ϕ . This implicit description has been shown to provide an automatic handling of complex topological deformations and numerical resolution. It also conveys smaller advantages such as the easy identification of the inside and outside of shapes through the sign of ϕ .

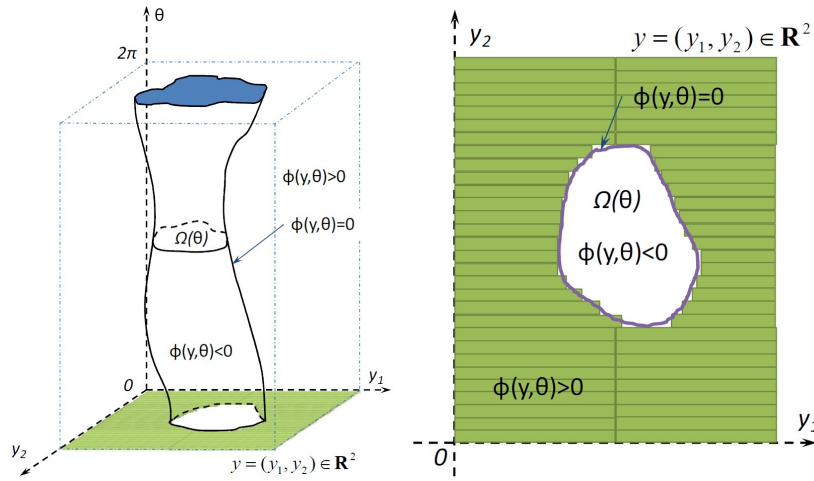


Figure 2.1: Left Figure: An illustration on formulating the VMAT optimization problem as a level-set problem: stacking the MLC apertures at all gantry angles together to form a cylinder-like shape in three dimensions. Right Figure: One MLC plane at a given gantry angle θ .

The binary version of the level-set representation restricts its level-set functions ϕ to take on only two values, usually -1 and 1 :

$$\phi : \mathbb{R}^2 \times [0, 2\pi] \rightarrow \{-1, 1\},$$

with the boundary of $\{(y, \theta) | \phi(y, \theta) < 0\}$ serving as the interface of interest. Such a restriction forces a very discrete interpretation of the problem since ϕ is no longer continuous; for example, numerically, subcell resolution is lost. Furthermore, much of the geometry of the surface of interest is lost as ϕ is no longer differentiable there. In spite of these concerns, the binary level-set method turns out to be suitable for our problem and further confers advantages of speed and simplicity.

Under this framework, with the binary level-set function ϕ representing aperture shapes, we arrive at the following form for our total energy:

$$E(\phi, s) = \frac{1}{2} \sum_{r=1}^{n_s} \int_{S_r} p_r \left(\int_0^{2\pi} \int_{\mathbb{R}^2} D(x, y, \theta) s(\theta) H(-\phi) dy d\theta \right) dx,$$

where H denotes the one-dimensional heaviside function.

2.3 Constraints

For our problem of interest, we must further restrict the attention of this energy to deliverable apertures and beam intensities due to constraints imposed by the equipment involved. We narrow our interest to three major constraints: a limit on how fast the beam can change its intensity during gantry rotation, how fast leaves of MLC can move during the rotation, and the aperture shapes allowed under MLC.

Let M be the given maximum allowable rate at which a beam can change intensity. Then our first constraint can be described by the equation

$$\left| \frac{d}{d\theta} s(\theta) \right| \leq M,$$

for all $\theta \in [0, 2\pi]$, which is a requirement on the beam intensity function s .

The remaining two constraints on aperture shapes arise from the physical setup of MLC, with its two banks of leaves that move back and forth to form an aperture. Let w denote a unit vector pointing in the direction the leaves of MLC are oriented. In this paper, we assume w is given and defer its optimization to future work. From this orientation, we know that deliverable aperture shapes must satisfy a directional-convexity requirement: $\phi(y, \theta) < 0$ and $\phi(y + \tau w, \theta) < 0$ for some y, θ and $\tau \in \mathbb{R}$ implies $\phi(y + \zeta w, \theta) < 0$ for any ζ between 0 and τ (see Figure 2.2).

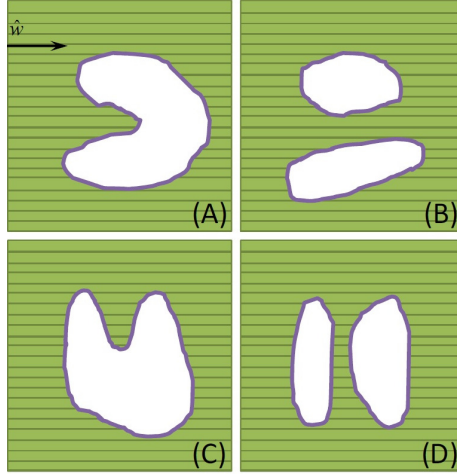


Figure 2.2: Illustration of deliverable apertures ((A) and (B)) and undeliverable ones ((C) and (D)) when leaves are oriented in the horizontal direction.

In addition, not allowing the leaves to move faster than some given value can be described mathematically as a bound on

$$\frac{|(\nabla\phi \times w^\perp) \cdot w|}{|(\nabla\phi \times w^\perp) \cdot e_3|},$$

at the aperture boundary, where ϕ here is the level-set function, rather than the binary level-set function, and w^\perp is a unit vector orthogonal to w . In practice, we will use a much simpler, discrete form of this constraint after discretization of the problem.

3 Algorithm

3.1 Discretization

Our first step in creating an algorithm to minimize the energy $E(\phi, s)$ is to discretize the problem. Let $x_i, i = 1, \dots, n_x$ be discrete locations in the patient's body, $y_j, j = 1, \dots, n_y$ those in the MLC plane, and $\theta_k, k = 1, \dots, n_\theta$ those for the gantry angle. We further require y_j and θ_k to be arranged as the gridpoints of a uniform grid over the MLC plane and $[0, 2\pi]$, respectively. Henceforth, we reserve the subscript i to relate to x_i , j to relate to y_j , and

k to relate to θ_k . Thus, ϕ_{jk} is the value of the binary level-set function ϕ at y_j and θ_k , s_k is the value of the beam intensity s at θ_k , z_i is the value of the dose distribution z at x_i , and D_{ijk} is the value of the dose deposition coefficient at x_i, y_j, θ_k . With these notations, we can write the discrete form of the total energy as

$$E(\phi_{jk}, s_k) = \frac{1}{2} \sum_{r=1}^{n_S} \sum_{i=1, x_i \in S_r}^{n_x} p_r(z_i),$$

where

$$z_i = \sum_{k=1}^{n_\theta} \sum_{j=1}^{n_y} D_{ijk} s_k H(-\phi_{jk}).$$

For a flow-based approach, we add iteration stage n , denoting by $\phi_{jk}^{(n)}$ and $s_k^{(n)}$ the values of the discrete level-set function and beam intensity, respectively, at this stage.

3.2 Aperture Part

3.2.1 Basic Outline

We first consider the case of a given and fixed beam intensity, thus allowing aperture shapes to play the main role in the energy. The main tool we use for this energy minimization is the switch, at a given point, of the sign of the binary level-set function, from -1 to 1 or from 1 to -1 .

For a fixed j^*, k^* , let $G_{j^*k^*}$ be the operator on discrete binary level-set functions that switches the sign at index j^*, k^* :

$$G_{j^*k^*} : \mathbb{R}^{n_y} \times \mathbb{R}^{n_\theta} \rightarrow \mathbb{R}^{n_y} \times \mathbb{R}^{n_\theta}$$

such that $\phi^* = G_{j^*k^*}(\phi)$ satisfies

$$\phi_{jk}^* = \begin{cases} -\phi_{j^*k^*}, & \text{if } j = j^*, k = k^* \\ \phi_{jk}, & \text{else.} \end{cases}$$

Physically, this switch represents the toggling of the state of the aperture, from open to closed or vice versa, at a chosen location in the MLC plane and a chosen gantry angle.

Use of this operator allows us to set up our basic outline for minimization: form a list of locations and for each one, switch the sign of the discrete

binary level-set function at that location if it yields a deliverable aperture shape with smaller energy. If, eventually, a switch at any location either increases the energy or produces an undeliverable aperture shape, then we accept the aperture shape of this final discrete binary level-set function to be at a local minimum of the energy. We flesh out this outline by filling in details concerning the procedure for checking for deliverable apertures and energy decrease, and the order and locations to include in the list.

3.2.2 Aperture Constraint Satisfaction

We begin by introducing a procedure for checking whether a given discrete binary level-set function represents a deliverable aperture shape in the simpler case of leaf orientation $w = (1, 0, 0)^t$. Given j, k , with j represented by $(j_1, j_2) \in \mathbb{R}^2$, we can extract the one-dimensional array of values of ϕ for j_1 varying and j_2, k fixed and compute, if they exist, the left-most index, call it $l_{j_2 k}$, and the right-most index, call it $r_{j_2 k}$, of those indices where $\phi < 0$. Directional-convexity simply needs to check whether $\phi < 0$ for indices $l_{j_2 k} < j_1 < r_{j_2 k}$, when the left- and right-most indices exist.

In fact, when directional-convexity is satisfied, $l_{j_2 k}$ and $r_{j_2 k}$ are simply the locations of the left and right leaf tips, respectively. Leaf speeds can be calculated by looking at these indices; for example, for the left leaf tip, we can compare the index of $l_{j_2 k}$ to those of $l_{j_2 \bar{k}}$, for \bar{k} nearby to k . If we agree to a discrete leaf speed limit, such as only allowing the leaf to move at most a index positions in the j_1 -direction every b index positions in the k -direction, we can formulate the condition: $\sum_{p=1}^b T_p \leq a$, where

$$T_p = \begin{cases} |l_{j_2, k+p-1} - l_{j_2, k+p}|, & \text{if } k+p \leq n_\theta \text{ and } l_{j_2, k+p-1}, l_{j_2, k+p} \text{ exist} \\ |r_{j_2, k+p-1} - l_{j_2, k+p-1}|/2, & \text{else if } k+p \leq n_\theta \text{ and } l_{j_2, k+p-1} \text{ exists} \\ |r_{j_2, k+p} - l_{j_2, k+p}|/2, & \text{else if } k+p \leq n_\theta \text{ and } l_{j_2, k+p} \text{ exists} \\ 0, & \text{else,} \end{cases}$$

with the middle two cases handling, though not perfectly, the cases where leaves are closed up and the left-most index does not exist. A similar condition can be formulated for the right leaf tips. Note $\sum_{p=1}^b T_p$ has a similar flavor as total variation.

We note that the computations involved in these checks of constraint satisfaction can be confined local to a change, such as our switch of sign performed at a single location, in a discrete binary level-set function with deliverable aperture shape.

3.2.3 Energy Decrease

We now consider an efficient procedure for checking energy decrease after a switch in sign of the discrete binary level-set function at a location. Let ϕ be a discrete binary level-set function and consider $\phi^* = G_{j^*k^*}\phi$, for some j^*, k^* . In addition, let z^* denote the dose distribution using ϕ^*, s . Then

$$z_i^* = \begin{cases} z_i - H(-\phi_{j^*k^*})D_{ij^*k^*}s_{j^*} + H(\phi_{j^*k^*})D_{ij^*k^*}s_{j^*}, & \text{if } D_{ij^*k^*} \neq 0 \\ z_i, & \text{else.} \end{cases}$$

So if we let

$$E_- = \frac{1}{2} \sum_{r=1}^{ns} \sum_{x_i \in S_r, D_{ij^*k^*} \neq 0} p_r(z_i)$$

$$E_+ = \frac{1}{2} \sum_{r=1}^{ns} \sum_{x_i \in S_r, D_{ij^*k^*} \neq 0} p_r(z_i^*),$$

then

$$E(\phi^*, s) = E(\phi, s) - E_- + E_+.$$

Now define $\delta E_{j^*k^*}(\phi, s)$ as the energy change due to a switch in sign of ϕ at j^*, k^* . Then

$$\delta E_{j^*k^*}(\phi, s) = E(\phi^*, s) - E(\phi, s) = -E_- + E_+.$$

Note, the number of operations needed for determining $\delta E_{j^*k^*}$ is on the order of the number of i such that $D_{ij^*k^*} \neq 0$.

3.2.4 List Ordering

The basic outline for our algorithm involves updating the aperture shape by changing the discrete binary level-set function location by location. Obviously, however, a switched sign at many locations would lead to a loss of directional-convexity. We thus restrict our attention to locations neighboring the aperture boundaries. This agrees with a flow-based strategy of boundary deformation and, in addition, significantly reduces the number of locations we need to consider in updating.

The greediest choice for ordering the locations would be to consider first the ones that, under a switch in sign, decrease the energy the most. Unfortunately, this turns out not to be efficient since it would require not only the

recomputation of energy changes at many locations every time a switch in sign is accepted, but also a re-sorting of these values to find the next location with largest decrease.

We instead compromise, decoupling the use of the energy change in determining the order of updating from its use in determining whether a switch in sign should be accepted. In detail, we calculate energy changes for all the locations neighboring the aperture boundary and then sort them so that those with the greatest decreases are at the head of the list. We then proceed through the entire list in this fixed order and, at each location, recompute the energy change of a switch of sign at that location. This is required because the sign switches accepted after the initial computation of energy changes may invalidate those values. The recomputed value can then be used to determine whether the current sign switch should be accepted. After going through the whole list, the process can be repeated and iterated, calculating energy changes at all locations to create the list and then individually recalculating at each location when going through the list.

3.2.5 Aperture Algorithm

We are finally ready to outline our flow-based, location-by-location, greedy algorithm for energy decrease in the case of a given and fixed beam intensity. Let $\phi^{(0)}$ be a given discrete binary level-set function representing an initial guess of a deliverable aperture shape and let $s^{(0)}$ be a given beam intensity. Our algorithm then proceed as follows:

1. Set $n := 0$ and compute the energy $E^{(0)} := E(\phi^{(0)}, s^{(0)})$.
2. Set $\phi^{(n+1)} := \phi^{(n)}$ and $E^{(n+1)} := E^{(n)}$.
3. For each location j, k neighboring the aperture boundary of $\phi^{(n+1)}$, compute and set $\delta E_{jk}^{(n+1)} := \delta E_{jk}(\phi^{(n+1)}, s^{(n)})$. Order these values in a heap.
4. Identify the location j^*, k^* with minimum value $\delta E_{j^*k^*}^{(n+1)}$ in the heap and calculate $\delta E_{j^*k^*}(\phi^{(n+1)}, s^{(n)})$.
5. If this value is negative and if, in addition, $G_{j^*k^*}(\phi^{(n+1)})$ represents a deliverable aperture shape, then set the new energy $E^{(n+1)} := E^{(n+1)} + \delta E_{j^*k^*}(\phi^{(n+1)}, s^{(n)})$ and the new discrete binary level-set function, $\phi^{(n+1)} := G_{j^*k^*}(\phi^{(n+1)})$.

6. Remove the minimum value from the heap and fix its ordering. Then return to step 4 unless the heap is empty.
7. Set $s^{(n+1)} := s^{(n)}$ and $n := n + 1$ and return to step 2.

Each iteration stage thus updates, if acceptable, all locations next to the aperture boundary of the previous stage. After our upcoming study of beam intensities that minimize the energy for fixed aperture shapes, we can modify the last step of this algorithm to set up such an iteration for s .

With the description of the aperture part of our algorithm completed, we can comment on the suitability of the binary level-set representation to our problem. With the binary representation, we do lose subcell accuracy in our aperture shapes and the leaf speed limit becomes harder to handle. However, first order accuracy and a discrete version of the constraint may be acceptable trade-offs given the benefits of a simplified setting and increased algorithmic speed.

3.3 Beam Intensity Part

3.3.1 Euler-Lagrange Equation

We now consider the case of a given and fixed discrete binary level-set function representing an aperture shape and allow the beam intensity to play the main role in minimizing the energy. We begin by solving for the Euler-Lagrange equation, which must be satisfied by a minimizer. Introducing the time parameter t into s , we get, formally:

$$\begin{aligned}
\frac{d}{dt}E(\phi, s) &= \frac{1}{2} \sum_{r=1}^{n_s} \frac{d}{dt} F_r(z) \\
&= \frac{1}{2} \sum_{r=1}^{n_s} \int_{S_r} \frac{d}{dt} p_r(z(x)) \, dx \\
&= \sum_{r=1}^{n_s} \int_{S_r} \frac{p'_r(z(x))}{2} z_t(x) \, dx,
\end{aligned}$$

where

$$\frac{1}{2} p'_r(z) = \begin{cases} \alpha_r(z - m_r) & \text{if } z \leq m_r \\ \beta_r(z - m_r) & \text{else.} \end{cases}$$

Note,

$$z_t(x) = \int_{\mathbb{R}^2} \int_0^{2\pi} D(x, y, \theta) H(-\phi(y, \theta)) \frac{d}{dt} s(\theta, t) d\theta dy,$$

and, thus,

$$\begin{aligned} \frac{d}{dt} E(\phi, s) &= \sum_{r=1}^{n_S} \int_{S_r} \frac{p'_r(z(x))}{2} \int_{\mathbb{R}^2} \int_0^{2\pi} D(x, y, \theta) H(-\phi(y, \theta)) \frac{d}{dt} s(\theta, t) d\theta dy dx \\ &= - \int_0^{2\pi} g(\theta, s(\theta, t)) \frac{d}{dt} s(\theta, t) d\theta, \end{aligned}$$

where

$$g(\theta, s) = - \sum_{r=1}^{n_S} \int_{S_r} \frac{p'_r(z(x))}{2} \int_{\mathbb{R}^2} D(x, y, \theta) H(-\phi(y, \theta)) dy dx.$$

The minimum is achieved when $\frac{d}{dt} E(\phi, s) = 0$ for arbitrary $\frac{d}{dt} s$ and so the minimizer satisfies $-g(\theta, s) = 0$ or, written out,

$$\sum_{r=1}^{n_S} \int_{S_r} \frac{p'_r(z(x))}{2} \int_{\mathbb{R}^2} D(x, y, \theta) H(-\phi(y, \theta)) dy dx = 0.$$

This final equation is the Euler-Lagrange equation.

In addition, gradient descent can be achieved through the flow

$$\begin{aligned} \frac{d}{dt} s(\theta, t) &= g(\theta, s(\theta, t)) \\ &= - \sum_{r=1}^{n_S} \int_{S_r} \frac{p'_r(z(x))}{2} \int_{\mathbb{R}^2} D(x, y, \theta) H(-\phi(y, \theta)) dy dx. \end{aligned}$$

Note this decreases the energy since s is not a minimizer implies $-g(\theta, s(\theta, t)) \neq 0$, and so

$$\frac{d}{dt} E(\phi, s) = - \int_0^{2\pi} (g(\theta, s(\theta, t)))^2 d\theta < 0$$

for continuous g . Note though s explicitly appears neither in the Euler-Lagrange nor the gradient descent equations, it is a hidden part of the dose distribution $z(x)$.

Discrete versions can also be written down, with the Euler-Lagrange equation taking the form

$$\sum_{r=1}^{n_S} \sum_{i=1}^{n_x} \frac{p'_r(z_i)}{2} \sum_{j=1}^{n_y} D_{ijk} H(-\phi_{jk}) = 0$$

and the gradient descent equation, under Euler's method on the differential equation, taking the form

$$s_k^{(n+1)} = s_k^{(n)} - \Delta t \sum_{r=1}^{n_S} \sum_{i=1}^{n_x} \frac{p'_r(z_i)}{2} \sum_{j=1}^{n_y} D_{ijk} H(-\phi_{jk}),$$

where Δt is a chosen stepsize in time and $s_k^{(n)}$ denotes the discrete beam intensity at time step n . We can iterate this gradient descent equation to convergence to minimize our energy; however, this solution will generally violate the constraint on how fast beam intensities can change as the gantry rotates.

3.3.2 Beam Intensity Constraint Conditions

In the presence of our beam intensity constraint, we seek to replace the gradient descent approach's rate of change, g , to preserve both energy decrease and constraint satisfaction. Under this new rate, the energy will decrease and, furthermore, if we start with an initial guess of the beam intensity that satisfies the constraint, the beam intensity will continue to satisfy the constraint for all time.

We start by considering a general differential equation on s of the form

$$\frac{d}{dt} s(\theta, t) = v(\theta, s(\theta, t)).$$

With this choice,

$$\frac{d}{dt} E(\phi, s) = - \int_0^{2\pi} g(\theta, s(\theta, t)) v(\theta, s(\theta, t)) d\theta,$$

which implies that if v satisfies $g(\theta, s(\theta, t)) v(\theta, s(\theta, t)) > 0$ when $g(\theta, s(\theta, t)) \neq 0$, then energy decrease is guaranteed. Furthermore, if $v(\theta, s(\theta, t)) = 0$ only

when $g(\theta, s(\theta, t)) = 0$, then if the differential equation converges, it will converge to the minimizer of the energy. Essentially, these conditions can be stated as: v has the same sign as g .

On the other hand, we also need to determine conditions on v to satisfy the constraint $|\frac{\partial}{\partial\theta}s(\theta, t)| \leq M$, for all θ and t , where M denotes the given maximum allowed rate for intensity change. Taking a derivative in θ on both sides of our flow equation yields

$$\frac{\partial^2}{\partial t \partial \theta} s(\theta, t) = \frac{d}{d\theta} [v(\theta, s(\theta, t))].$$

Suppose the constraint is satisfied initially, $|\frac{\partial}{\partial\theta}s(\theta, 0)| \leq M$ for all θ . Then by imposing $\frac{\partial^2}{\partial t \partial \theta} s(\theta, t) \leq 0$ when $\frac{\partial}{\partial\theta}s(\theta, t) \geq M$ and $\frac{\partial^2}{\partial t \partial \theta} s(\theta, t) \geq 0$ when $\frac{\partial}{\partial\theta}s(\theta, t) \leq -M$, the constraint $|\frac{\partial}{\partial\theta}s(\theta, t)| \leq M$ will continue to be satisfied for all θ, t . This translates to conditions on v :

$$\begin{cases} \frac{d}{d\theta} [v(\theta, s(\theta, t))] \leq 0, & \text{if } \frac{\partial}{\partial\theta}s(\theta, t) \geq M \\ \frac{d}{d\theta} [v(\theta, s(\theta, t))] \geq 0, & \text{if } \frac{\partial}{\partial\theta}s(\theta, t) \leq -M. \end{cases}$$

Construction of such a v that, in addition, has the same sign as g produces a flow that both decreases energy and preserves constraint satisfaction.

3.3.3 Enforcing Beam Intensity Constraints

We present here a construction of such a v using eikonal equation theory. Fixing t and given $s(\theta, t)$, we can solve for v as a function of θ , with the same sign as g , from the eikonal equation

$$\left| \frac{d}{d\theta} v \right| = H \left(M - \left| \frac{d}{d\theta} s(\theta, t) \right| \right),$$

where H is once again the one-dimensional heaviside function. Thus the right hand side is either 1 or 0 depending on whether $|\frac{d}{d\theta}s(\theta, t)| \leq M$ is satisfied or not.

In the discrete setting, we choose to recompute the discrete version of the eikonal equation from a discrete flow and constraints. The discrete version of our flow, $\frac{d}{dt}s(\theta, t) = v(\theta, s(\theta, t))$ can be written, under Euler's method, as

$$s_k^{(n+1)} = s_k^{(n)} + \Delta t v_k^{(n)},$$

where $v_k^{(n)}$ refers to $v(\theta_k, s_k^{(n)})$. Furthermore, the discrete version of our constraint on beam intensities can be written as

$$|s_{k+1}^{(n)} - s_k^{(n)}|/\Delta\theta \leq M$$

for all n , where $\Delta\theta$ is the stepsize of our discretization in the θ -direction. Then following a discrete version of our previous argument, $|s_{k+1}^{(n+1)} - s_k^{(n+1)}|/\Delta\theta \leq M$ is satisfied when

$$M_1 \leq \frac{v_{k+1}^{(n)} - v_k^{(n)}}{\Delta\theta} \leq M_2,$$

where

$$\begin{aligned} M_1 &= \frac{1}{\Delta t} \left(-M - \frac{s_{k+1}^{(n)} - s_k^{(n)}}{\Delta\theta} \right) \\ M_2 &= \frac{1}{\Delta t} \left(M - \frac{s_{k+1}^{(n)} - s_k^{(n)}}{\Delta\theta} \right). \end{aligned}$$

Note $M_1 \leq 0 \leq M_2$ if $|s_{k+1}^{(n)} - s_k^{(n)}|/\Delta\theta \leq M$. Thus we choose to construct $v^{(n)}$, with the same sign as $g^{(n)}$, from the equations

$$\begin{cases} \frac{v_{k+1}^{(n)} - v_k^{(n)}}{\Delta\theta} = \min\{1, M_2\}, & \text{if } v_{k+1}^{(n)} \geq v_k^{(n)} \\ \frac{v_{k+1}^{(n)} - v_k^{(n)}}{\Delta\theta} = \max\{-1, M_1\}, & \text{else.} \end{cases}$$

We modify an eikonal equation solver called the fast sweeping method [25, 26], a variant of the fast marching method [27–29], to handle these equations. This modified algorithm, in our one-dimensional setting, is as follows:

1. For $k = 1, \dots, n_\theta$, set

$$v_k^{(n)} := \begin{cases} \infty, & \text{if } g_k^{(n)} > 0 \\ -\infty, & \text{else.} \end{cases}$$

2. For $k = 1, \dots, n_\theta$, compute $v_k^{(n)}$ as follows: first, for $j = k - 1, k + 1$, set

$$a_{kj} := \begin{cases} \min\{1, M_1\}, & \text{if } (k - j)g_k^{(n)} > 0 \\ \max\{-1, M_2\}, & \text{else.} \end{cases}$$

Now, for $j = k - 1, k + 1$, set

$$b_{kj} := \begin{cases} v_{k-1}^{(n)} + a_{kj}\Delta\theta, & \text{if } g_k^{(n)}g_j^{(n)} > 0 \\ -a_{kj}g_k^{(n)}(k-j)/(g_k^{(n)} - g_j^{(n)})\Delta\theta, & \text{else.} \end{cases}$$

Finally, for $j = k - 1, k + 1$, set

$$v_k^{(n)} := \begin{cases} \min\{b_{k,k-1}, b_{k,k+1}\}, & \text{if } k - 1 \geq 0, k + 1 \leq n_\theta \\ b_{k,k-1}, & \text{if } k + 1 > n_\theta \\ b_{k,k+1}, & \text{if } k - 1 < 0. \end{cases}$$

3. Repeat step 2 for $k = n_\theta, \dots, 1$.
4. For a given $C > 0$, set $v_k^{(n)} := \min\{\max\{v_k^{(n)}, C\}, -C\}$.

We add the last step to allow a threshold of $v_k^{(n)}$ so that $s_k^{(n)}$ will not grow at very different rates at different locations of k . This final computed $v^{(n)}$ allows $s^{(n+1)}$ in the discrete flow to preserve constraint satisfaction for the beam intensity while decreasing the energy.

Figure 3.1 shows visually how the fast sweeping algorithm works to solve the standard eikonal equation $|\nabla s| = 1$, which represents the case with no bounds on speed limits: $M_1 = -\infty, M_2 = \infty$. The given function in the first panel is first replaced by the values $\pm\infty$ or 0 while preserving the sign, as shown in the second panel. The third panel shows the first of two sweeps in the method. Enacting changes from left to right, lines of slope ± 1 are created from the zeros and replace previous values with larger magnitudes. The fourth panel then shows the second sweep in the process. Enacting changes this time from right to left, lines of slope ± 1 are created from the zeros and replace previous values of larger magnitudes while being replaced by previous values of smaller magnitudes. The fifth panel shows the resulting function s satisfying $|\nabla s| = 1$ and with the same sign as the given function of the first panel. The case of finite M_1 and M_2 behaves similarly but with lines of different slopes.

3.3.4 Beam Intensity Algorithm

For the final and complete algorithm, the one minimizing our total energy with respect to both aperture shapes and beam intensity, and satisfying our chosen constraints, we modify certain steps of and add certain steps to our

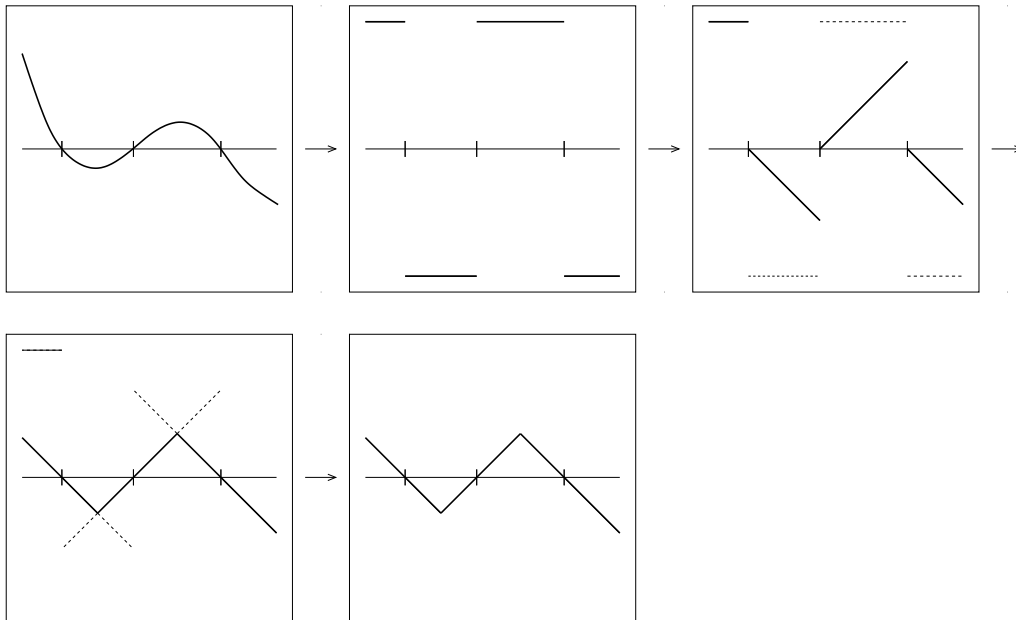


Figure 3.1: Fast sweeping process for the standard eikonal equation. The dashed lines indicate values that were calculated but replaced or rejected because a value with smaller magnitude was available.

aperture algorithm. To begin, we additionally require the starting beam intensities to be deliverable. Then we remove the last step of the aperture algorithm and add our beam intensity contributions:

7. Solve for $v_k^{(n)}$ using our modified fast sweeping algorithm.
8. Solve for $s_k^{(n+1)}$ using Euler's method with $v_k^{(n)}$ and a chosen Δt .
9. Return to step 8 with a smaller Δt if the energy $E(\phi^{(n+1)}, s^{(n+1)})$ is not decreased.
10. Set $n = n + 1$ and return to step 2.

Note, since the aperture part of our algorithm ensures energy decrease, we include step 9 to preserve this property, knowing it is satisfied as $\Delta t \rightarrow 0$.

Thus, in whole, we see that the final algorithm takes turns, first fixing beam intensity and optimizing with respect to aperture shapes, then fixing the aperture shape and optimizing with respect to beam intensity. This process is then repeated until convergence, at which point we accept the final aperture shape and beam intensity as approximate minimizers.

We now need to study the actual abilities of this completed algorithm, including its speed, memory usage, the aperture shapes and beam intensities it returns and the dose distributions they form.

4 Results

4.1 Dose-Volume Histogram

One option we have in viewing the quality of a given dose distribution is to overlay the dosage levels over imaging scans of the body area of interest and eyeball the results. This approach can give valuable qualitative information but is lacking in delivering quantitative information. Furthermore, it actually is not so easy to visualize the three-dimensional results. We do provide some of this visualization by showing the results on some chosen two-dimensional slices; however, for a more quantitative approach, we turn to the dose-volume histogram.

Given a structure S , such as an organ, a dose distribution z , and a dose level m , consider the probability density function given by

$$p(\zeta) = \frac{1}{\text{vol}(S)} \int_S \delta(z(x) - \zeta) dx,$$

where δ is the one-dimensional delta function. The DVH function can then be defined as

$$\begin{aligned} \text{DVH}(m) &= \int_m^\infty p(\zeta) d\zeta = \frac{1}{\text{vol}(S)} \int_S H(z(x) - m) dx \\ &= \frac{\text{vol}(\{x|z(x) \geq m\})}{\text{vol}(S)} \end{aligned}$$

for that structure. Thus $\text{DVH}(m)$ reveals the percentage of the structure that is irradiated at or above the dose level m . For a target structure, the optimal DVH profile is a step function that is at 100% before the prescription dose and 0% afterwards. For a critical structure, the optimal DVH profile is a function that is at 0% after the safe dose limit for the particular tissue involved.

4.2 Tests

4.2.1 Model Cases

We first test constraint satisfaction of our algorithm in a partly manufactured example that uses as a basis real data in a case of prostate cancer. In this test, we divide the 360° gantry rotation into 180 equally spaced 6 MV beams and take beamlet sizes of $10 \times 10 \text{ mm}^2$ for discretization of the MLC plane and voxel sizes of $2.5 \times 2.5 \times 2.5 \text{ mm}^3$ for discretization of the patient's target and critical structures. The manufactured part of our test involves our choice of non-realistic constraint parameters that instead emphasize and display constraint satisfaction and, as a bonus, energy decrease.

Figure 4.1 shows an example where leaf and beam intensity speed are purposely overly restricted, for clarity in the results. The upper-left plot in the figure shows the zero level-set surface plotted in $\mathbb{R}^2 \times [0, 2\pi]$. Note the restriction on the speed the surface can change in the vertical direction, the direction of the gantry angle θ , due to the speed limit for leaves. The upper-right plot shows the aperture shapes for a few chosen angles. Note that directional-convexity, in this case in the horizontal direction, is satisfied for each shape. The lower-left plot then shows a graph of beam intensity where we can plainly see the restriction on the first derivative. Finally, the lower-right plot shows the energy profile over 120 iterations. Note the monotonic decrease forced by our approach.

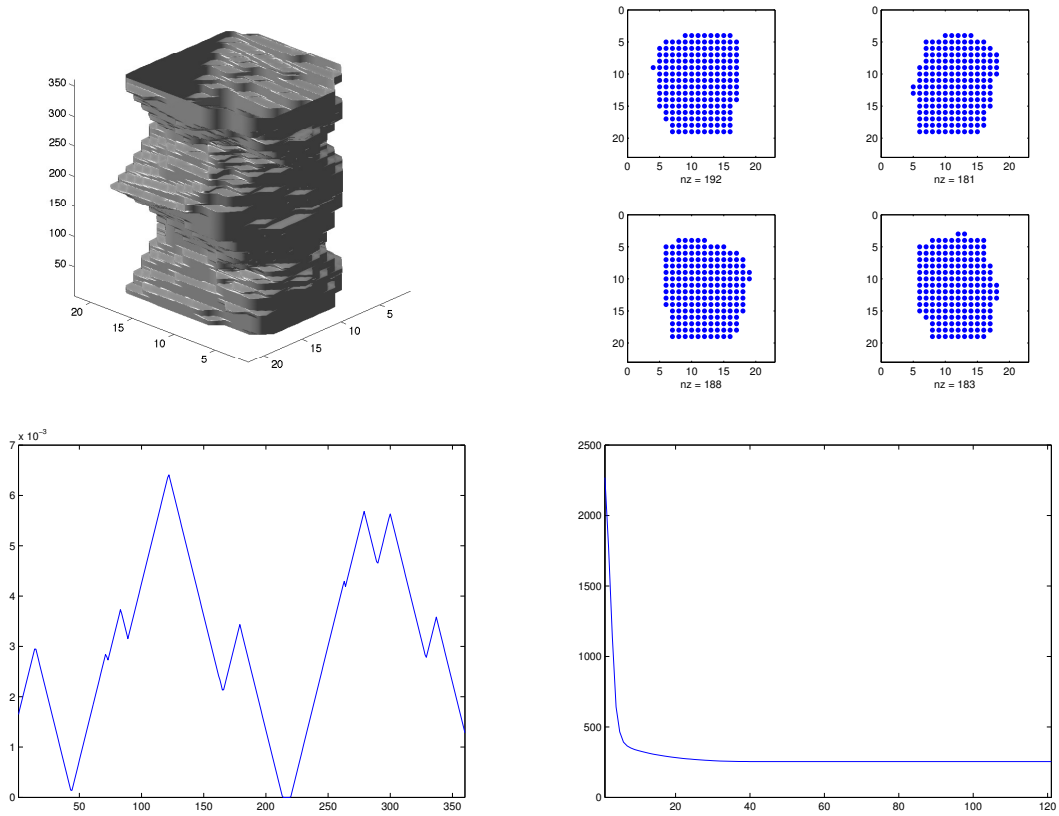


Figure 4.1: A collection of results of zero level-set surface (upper-left), individual aperture shapes (upper-right), beam intensity (lower-left), and energy profile (lower-right).

Each iteration took around 3 to 3.5 seconds and the total runtime for the program was around 6 minutes. We expect, however, that we can reduce this runtime with optimized programming and a better convergence criterion, since convergence seems to have been achieved before the 120th iteration.

We also present in Figure 4.2 the DVH plot of our tests in a different example that considers just two structures, one a target structure and one a critical structure. In this case, we chose to irradiate the target structure to 77.4 Gy and wanted to keep the critical structure below 23.52 Gy in dosage. From the figure, we see our algorithm can largely obey these requirements, with around 90% of the target structure dosed at 77.4 Gy and only around 10% of the critical structure dosed above 23.52 Gy. We note our own tests and those of other algorithms, presented later in the paper, seem to show that it is near impossible to get perfect results, with 100% of the target structures dosed at their desired limits and 0% of the critical structures dosed above their safe limits. Our DVH curves, however, will generally take on the desired form with curves related to target structures far to the right and curves related to critical structures far to the left, as demonstrated in our figure for this model example.

4.2.2 Clinical Cases

We now test our algorithm with data collected from actual clinical cases of cancer. In all, we have tested five cases of prostate cancer and five cases of head-and-neck cancer and, since results were mostly similar, we present in detail one representative case from each setting. Images and graphs showing the results of our algorithm are presented in Figures 4.3, 4.4, and 4.5. Additional images and graphs are included to verify the quality of our results through a comparison with those of another current approach in radiotherapy. We note that our approach does involve trial-and-error tweaking of penalty constants in our energy to present the best results.

The first test we consider is a case of prostate cancer, where the target, PTV or planning target volume, consists of a slight enlargement of the gross tumor volume (GTV) to account for both sub-clinical disease as well as daily setup errors and internal organ motion. For this region, we prescribe a dose of 73.8 Gy for elimination of the cancerous growth. Safe dose limits of 23.52 Gy and 32.92 Gy are further prescribed, respectively, for the nearby critical structures of the bladder and rectum.

Figure 4.3 shows the results of our algorithm. We note the DVH curves

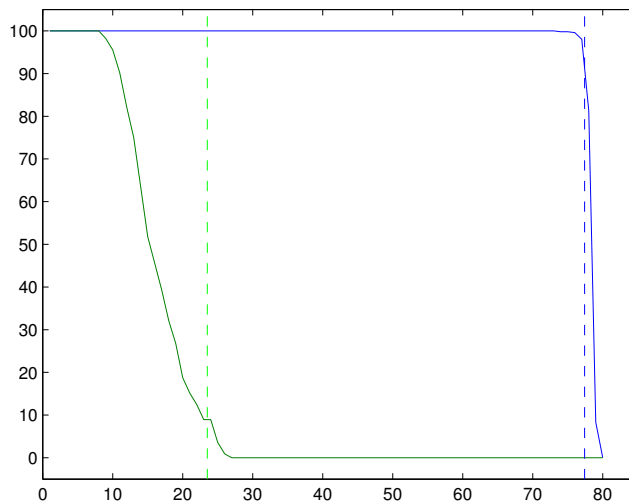


Figure 4.2: DVH plot of a model case with one target structure and one critical structure, with dashed lines showing the desired and safe limits for each structure’s dosage.

have the desired form of high doses applied to target structures and low doses to critical structures. In fact, the target is pretty much completely dosed at or above the required level. In the critical structures, on the other hand, roughly 70% of the bladder and 75% of the rectum are dosed below their safe limits. Since these results by themselves may seem poor, we include in the plots results, for comparison, from another algorithm currently used in radiotherapy that is built on the IMRT setup. This comparison shows that our results are actually very good, with both algorithms applying similarly high doses to the target but with ours applying much lower doses to the critical structures.

A particular slice of the patient’s scan is also given in the figure, with dose distributions and their level-sets overlaying the outlined prostate and other organs. We get from this image visual confirmation of high doses being applied to the target and low doses to the rest of the region. We also see that the dose distribution generated from our algorithm is different from that of the IMRT algorithm, which is also given for comparison.

Finally, Figure 4.4 shows a sampling of the apertures and the beam in-

tensities calculated by our algorithm for this problem.

For the second of our clinical tests, we tackle a more complicated case of cancer in the head-and-neck region. This case involves two different PTV regions, labeled PTV1 and PTV2. PTV1 once again expands on the GTV, which consists of two connected components of tumors, and a prescription dose of 73.8 Gy is chosen for it. PTV2, however, comprises a larger target area that additionally contains nearby high-risk nodal regions. We choose a different prescription dose of 54 Gy for this target. Critical structures include the submandibular gland and parotid gland which again have dose limits around the range of 20 or 30 Gy.

Figure 4.5 shows the results of our algorithm in this case, along with the results of an IMRT algorithm for comparison. Once again, images are presented overlaying dosages and their level-sets on a particular slice of a scan of the patient’s head and neck region with circled structures. These images show though both our algorithm and the IMRT algorithm are applying higher doses of radiation to the target structures, they are different in the rest of the distribution of the doses.

For a more detailed look at how the doses are affecting the structures of interest, we turn to the DVH plot. This plot definitively shows the target structures receiving similarly high doses from both algorithms and critical structures receiving lower doses, which is the desired form. Our algorithm, however, seems to be applying lower doses to a greater volume of the critical structures. Thus, our results, once again, are better than those of the competing IMRT algorithm.

Figure 4.4 additionally shows a sampling of the apertures and the beam intensities calculated by our algorithm for this problem.

From these tests on clinical cases of cancer, we see that our algorithm has the desired characteristics of a good treatment plan, with high doses applied to target structures and low doses applied to critical structures. Furthermore, our dose distributions are different from those of other algorithms and in many situations show critical structures receiving less dosage.

5 Conclusion

In summary, we have in this paper developed a variational model and the associated numerical techniques for optimization of VMAT treatment plans in cancer radiotherapy. Our variational model places the problem in a

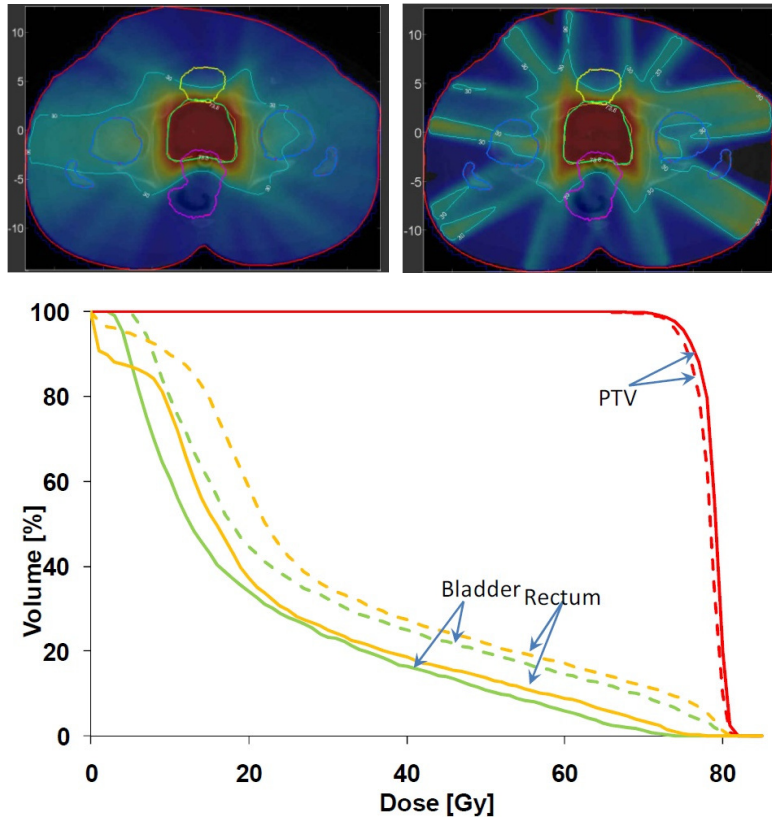


Figure 4.3: Results of a VMAT plan created by our algorithm shown against those of another algorithm using the IMRT setup in a clinical case of prostate cancer. The first row shows our dose distributions (left) and those of the IMRT algorithm (right), with dose amounts (red for high, blue for low) and their level-sets overlaid on a chosen slice of a patient's scan with structures of interest circled. The second row shows the DVH curves for our algorithm (solid lines) and those of the IMRT algorithm (dashed lines).

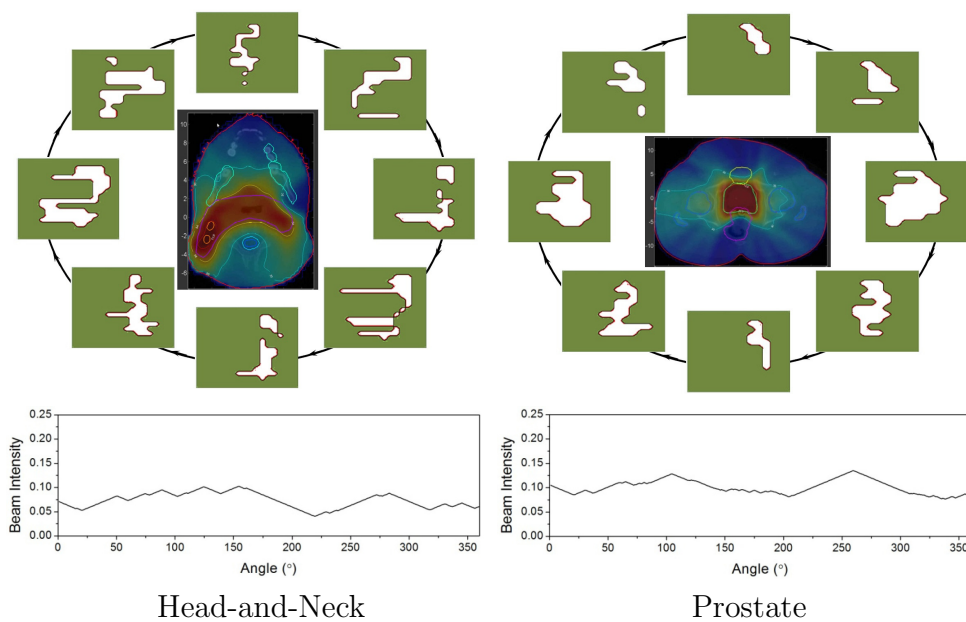


Figure 4.4: The beam apertures during the gantry rotation and the beam intensities for the VMAT plans computed by our algorithm in the case of prostate cancer (left) and head-and-neck cancer (right). Note in these two cases, the leaves are oriented in the horizontal direction.

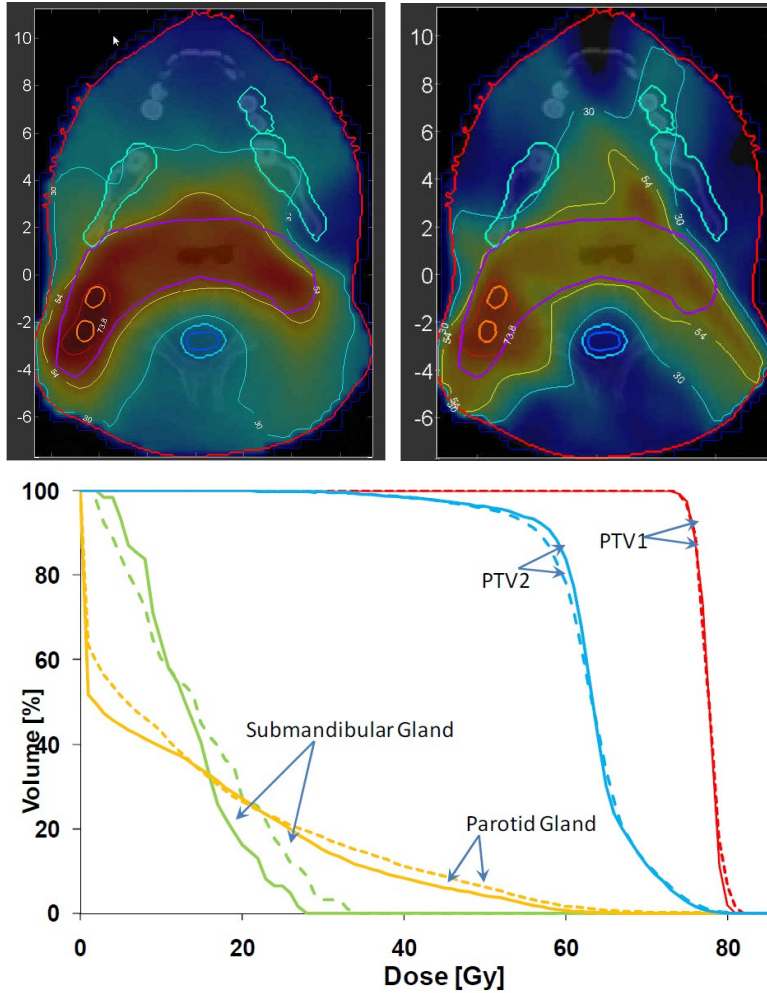


Figure 4.5: Results of a VMAT plan created by our algorithm shown against those of another algorithm using the IMRT setup in a clinical case of head-and-neck cancer. The first row shows our dose distributions (left) and those of the IMRT algorithm (right), with dose amounts (red for high, blue for low) and their level-sets overlaid on a chosen slice of a patient’s scan with structures of interest circled. The second row shows the DVH curves for our algorithm (solid lines) and those of the IMRT algorithm (dashed lines).

framework that allows the use of mathematical techniques such as the level-set method for shape optimization. We adopted the binary version of this method, with advantages in speed and simplicity for the aperture part of the optimization, and a modified gradient descent approach for the intensity part. For each, we listed in detail the steps involved, ultimately creating a complete algorithm with characteristics of guaranteed energy decrease and constraint satisfaction, discrete in the case of apertures. We then conducted tests verifying constraint satisfaction and studying the quality of our computed dose distributions with some comparisons to existing algorithms in clinical cases of cancer. These tests revealed that our algorithm shows great promise in the generation of desired dose distributions for treatment plans in cancer radiotherapy.

Much future work remains, though, in further preparing our approach for real-world use. This includes the need for experiments on more clinical cases; the addition of more freedoms and constraints that arise, for example, in generalizing MLC orientations and gantry rotations; and more investigations into desired forms for the energy and its minimization such as including various penalty constants into the optimization and a look into partial convexification of the energy for global minimization. Thus, we believe we have created an algorithm that represents a strong first step in a new direction and hope that future work can allow this direction to realize the full potential of VMAT in cancer radiotherapy.

6 Acknowledgements

This work was supported in part by the National Institutes of Health (NIH) through the grant R01GM096188 (L.-T. Cheng) and by Varian Medical Systems, Inc. (Steve B. Jiang).

References

- [1] S. Luan, C. Wang, D. Cao, D. Chen, D. Shepard, and C. Yu, “Leaf-sequencing for intensity-modulated arc therapy using graph algorithms,” *Medical physics*, vol. 35, p. 61, 2008.
- [2] K. Otto, “Volumetric modulated arc therapy: IMRT in a single gantry arc,” *Medical physics*, vol. 35, p. 310, 2008.

- [3] C. Wang, S. Luan, G. Tang, D. Chen, M. Earl, and C. Yu, “Arc-modulated radiation therapy: a single-arc form of intensity-modulated arc therapy,” *Physics in medicine and biology*, vol. 53(22), pp. 6291–6303, 2008.
- [4] K. Bzdusek, H. Friberger, K. Eriksson, B. Hårdemark, D. Robinson, and M. Kaus, “Development and evaluation of an efficient approach to volumetric arc therapy planning,” *Medical physics*, vol. 36, p. 2328, 2009.
- [5] G. Tang, M. Earl, and C. Yu, “Variable dose rate single-arc IMAT delivered with a constant dose rate and variable angular spacing,” *Physics in Medicine and Biology*, vol. 54, p. 6439, 2009.
- [6] A. Fogliata, A. Clivio, G. Nicolini, E. Vanetti, and L. Cozzi, “Intensity modulation with photons for benign intracranial tumours: A planning comparison of volumetric single arc, helical arc and fixed gantry techniques,” *Radiotherapy and Oncology*, vol. 89, no. 3, pp. 254–262, 2008.
- [7] D. Palma, E. Vollans, K. James, S. Nakano, V. Moiseenko, R. Shaffer, M. McKenzie, J. Morris, and K. Otto, “Volumetric modulated arc therapy for delivery of prostate radiotherapy: Comparison with intensity-modulated radiotherapy and three-dimensional conformal radiotherapy,” *International journal of radiation oncology, biology, physics*, vol. 72, no. 4, pp. 996–1001, 2008.
- [8] F. Kjær-Kristoffersen, L. Ohlhues, and J. Medin, “RapidArc volumetric modulated therapy planning for prostate cancer patients,” *Acta Oncologica*, vol. 48, no. 2, pp. 227–232, 2009.
- [9] L. Masi, F. Casamassima, R. Doro, A. Colantuoni, I. Bonucci, and C. Menichelli, “VMAT Plans Solution with Single and Double Gantry Rotation Compared with IMRT Step & Shoot for Different Treatment Sites,” *International Journal of Radiation Oncology* Biology* Physics*, vol. 75, no. 3, pp. S706–S707, 2009.
- [10] R. Shaffer, W. Morris, V. Moiseenko, M. Welsh, C. Crumley, S. Nakano, M. Schmuland, T. Pickles, and K. Otto, “Volumetric modulated arc therapy and conventional intensity-modulated radiotherapy for simultaneous maximal intraprostatic boost: a planning comparison study,” *Clinical Oncology*, vol. 21, no. 5, pp. 401–407, 2009.

- [11] T. Bortfeld, “The number of beams in IMRT theoretical investigations and implications for single-arc IMRT,” *Physics in Medicine and Biology*, vol. 55, p. 83, 2010.
- [12] C. Popescu, E. Wai, W. Ansbacher, L. Salter, I. Olivotto, W. Beckham, and K. Otto, “Volumetric Modulated Arc Therapy (VMAT) Improves Dosimetry and Reduces Treatment Time Compared to 9-field Conventional Intensity Modulated Radiotherapy (cIMRT) for Locoregional Radiotherapy of Left-sided Breast Cancer,” *International Journal of Radiation Oncology* Biology* Physics*, vol. 72, no. 1, p. S521, 2008.
- [13] R. Shaffer, A. Nichol, E. Vollans, M. Fong, S. Nakano, V. Moiseenko, M. Schmuland, R. Ma, M. McKenzie, and K. Otto, “A Comparison of Volumetric Modulated Arc Therapy and Conventional Intensity-Modulated Radiotherapy for Frontal and Temporal High-Grade Gliomas,” *International Journal of Radiation Oncology* Biology* Physics*, 2009.
- [14] G. Tang, M. Earl, S. Luan, C. Wang, M. Mohiuddin, and C. Yu, “Comparing Radiation Treatments Using Intensity-Modulated Beams, Multiple Arcs, and Single Arcs,” *International Journal of Radiation Oncology* Biology* Physics*, vol. 76, no. 5, pp. 1554–1562, 2010.
- [15] P. Zhang, L. Happersett, M. Hunt, A. Jackson, M. Zelefsky, and G. Mageras, “Volumetric Modulated Arc Therapy: Planning and Evaluation for Prostate Cancer Cases,” *International Journal of Radiation Oncology* Biology* Physics*, 2009.
- [16] S. Crooks, X. Wu, C. Takita, M. Watzich, and L. Xing, “Aperture modulated arc therapy,” *Physics in Medicine and Biology*, vol. 48, pp. 1333–1344, 2003.
- [17] C. Cameron, “Sweeping-window arc therapy: an implementation of rotational IMRT with automatic beam-weight calculation,” *Physics in medicine and biology*, vol. 50, p. 4317, 2005.
- [18] G. Tang, M. Earl, S. Luan, S. Naqvi, and C. Yu, “Converting Multiple-Arc Intensity Modulated Arc Therapy Into a Single Arc for Efficient Delivery,” *International Journal of Radiation Oncology* Biology* Physics*, vol. 69, no. 3, p. S673, 2007.

- [19] S. Ulrich, S. Nill, and U. Oelfke, “Arc-modulated cone beam therapy,” *Physics in medicine and biology*, vol. 52, pp. 4099–4119, 2007.
- [20] F. Gibou and R. Fedkiw, “A fast hybrid k-means level set algorithm for segmentation,” pp. 281–291, 2005.
- [21] B. Song and T. Chan, “A fast algorithm for level set based optimization,” *UCLA Cam Report*, vol. 2, p. 68, 2002.
- [22] J. Lie, M. Lysaker, and X.-C. Tai, “A variant of the level set method and applications to image segmentation,” *Math. Comp.*, vol. 75, no. 255, pp. 1155–1174, 2006.
- [23] S. Osher and J. Sethian, “Fronts propagating with curvature-dependent speed- Algorithms based on Hamilton-Jacobi formulations,” *Journal of Computational Physics*, vol. 79, pp. 12–49, 1988.
- [24] S. Osher and R. Fedkiw, “Level set methods: An overview and some recent results,” *Journal of Computational Physics*, vol. 169, pp. 463–502, Jan 2001.
- [25] Y. Tsai, L. Cheng, S. Osher, and H. Zhao, “Fast sweeping algorithms for a class of Hamilton-Jacobi equations,” *SIAM journal on numerical analysis*, vol. 41, no. 2, pp. 673–694, 2004.
- [26] H. Zhao, “A fast sweeping method for eikonal equations,” *Mathematics of computation*, vol. 74, no. 250, pp. 603–628, 2005.
- [27] J. HELMSEN, E. PUCKETT, P. COLELLA, and M. DORR, “Two new methods for simulating photolithography development in 3D,” vol. 2726, pp. 253–261, 1996.
- [28] J. Sethian, “A fast marching level set method for monotonically advancing fronts,” *Proceedings of the National Academy of Sciences*, vol. 93, no. 4, pp. 1591–1595, 1996.
- [29] J. Tsitsiklis, “Efficient algorithms for globally optimal trajectories,” *IEEE Transactions on Automatic Control*, vol. 40, no. 9, pp. 1528–1538, 1995.